Regulation of plant cell wall stiffness by mechanical stress: a mesoscale physical model

Hadrien Oliveri, Jan J. Traas, Christophe Godin, Olivier Ali

Regulation of plant cell wall stiffness by mechanical stress: a mesoscale physical model

Hadrien Oliveri · **Jan Traas** · **Christophe Godin**[*] · **Olivier Ali**[*]

Abstract A crucial question in developmental biology is how cell growth is coordinated in living tissue to generate complex and reproducible shapes. We address this issue here in plants, where stiff extracellular walls prevent cell migration and morphogenesis mostly results from growth driven by turgor pressure. How cells grow in response to pressure partly depends on the mechanical properties of their walls, which are generally heterogeneous, anisotropic and dynamic. The active control of these properties is therefore a cornerstone of plant morphogenesis.

Here, we focus on wall stiffness, which is under the control of both molecular and mechanical signaling. Indeed, in plant tissues, the balance between turgor and cell wall elasticity generates a tissue-wide stress field. Within cells, mechanosensitive structures, such as cortical microtubules, adapt their behavior accordingly and locally influence cell wall remodeling dynamics. To fully apprehend the properties of this feedback loop, modeling approaches are indispensable. To that end, several modeling tools in the form of virtual tissues have been developed. However, these models often relate mechanical stress and cell wall stiffness in relatively abstract manners, where the molecular specificities of the various actors are not fully captured.

In this paper, we propose to refine this approach by including parsimonious biochemical and biomechanical properties of the main molecular actors involved. Through a coarse-grained approach and through finite element simulations, we study the role of stress-sensing microtubules on organ-scale mechanics.

[*]Corresponding authors: christophe.godin@inria.fr (CG), olivier.ali@inria.fr (OA)

ORCID: 0000-0002-5488-5567 (HO), 0000-0001-5107-1472 (JT), 0000-0002-1202-8460 (CG), 0000-0001-7671-7225 (OA)

Laboratoire Reproduction et Développement des Plantes, Univ Lyon, ENS de Lyon, UCB Lyon 1, CNRS, INRA, Inria, F-69342, Lyon, France

Main quantities

L_g	Growth rate tensor
E	Elastic strain tensor
S	Stress tensor
Φ	Cell wall extensibility
τ	Cell wall yield strain
$\mathbb{C}_w$	Cell wall stiffness tensor
$\mathbb{C}_g$	Stiffness tensor associated with the wall's isotropic matrix
$\mathbb{C}_f$	Stiffness tensor associated with microfibrils
Y, ν	Wall matrix reduced Young's modulus and Poisson's ratio
Y_f	Microfibril reduced Young's modulus
θ	Angle parameter in the wall tangential plane
e_θ	Unit vector oriented by θ
Θ	Projector on span (e_θ)
$\rho(\theta)$	Angular density of microfibrils
$\phi(\theta)$	Angular density of microtubules
$f(\theta)$	Angular density of force (per unit surface)
$\hat{\rho}_n$, ρ_n, $\tilde{\rho}_n$	Complex, even and odd Fourier coefficients of ρ
$\hat{\phi}_n$	Complex Fourier coefficients of ϕ
$\hat{f}_n$	Complex Fourier coefficients of f
α_ρ	Anisotropy of microfibrils
α_ϕ	Anisotropy of microtubules
α_f	Anisotropy of forces
k_ρ, k'_ρ	Microfibril polymerization and depolymerization constants
k_ϕ	Microtubule polymerization constant
k'^{0}_ϕ	Inverse of stress-free microtubule half-life
γ	Coupling coefficient of the stress-induced microtubule stabilization
$k'_\phi(\theta) = k'^{0}_\phi e^{-\gamma f(\theta)}$	Angular microtubule depolymerization coefficient
c_0	Total concentration of tubulin
K_ρ, K_ϕ	Equilibrium constants of the microfibril/microtubule kinetics
η	Measure of the relative stiffness between the gel and the fiber

1 Introduction

In the absence of cell migration, plant development occurs through inhomogeneous and anisotropic irreversible deformations of the tissue, driven by turgor-induced forces. It has been proposed that global shape changes are controlled locally, at the cellular level, through three geometric parameters: growth rate, growth direction, and the degree of growth anisotropy (Erickson, 1976; Coen et al, 2004; Kennaway et al, 2011). How individual cells regulate these parameters is fundamental to understanding how plants control their shape.

Growth results from turgor-induced forces, that are counterbalanced by the cell wall, a stiff exoskeleton surrounding the cells and preventing them from bursting (Hamant and Traas, 2010). The wall is a complex assembly of cellulose microfibrils cross-linked by a network of polysaccharides, including hemicelluloses and pectins (Cosgrove, 2001). When stretched above a certain threshold these cross-links may

break, allowing microfibrils to slide (as modeled in Dyson et al, 2012) thus causing the irreversible expansion of the wall. New material is simultaneously added to maintain wall integrity (Cosgrove, 2005). This irreversible process defines cell growth. Throughout development, cells may have different growth rates at different positions and times. In addition, since microfibrils can be deposited in more or less parallel arrays, and/or because the wall may be mechanically stressed unequally in various directions, cell growth may be anisotropic (Fig. 1(a) Baskin, 2005).

The central role of wall mechanics in growth has motivated the development of a *rheological* formalization of tissue expansion, initiated by Lockhart on one-dimensional (1D) cell expansion (Lockhart, 1965; Ortega, 1985). In brief, Lockhart modeled the cell wall as a Bingham plastic undergoing linear irreversible expansion above a certain yield pressure. In recent years, computational modeling has been used to represent higher-dimensional tissue expansion, in 2D or 3D (for a review see Ali et al, 2014). Several studies were based on discrete tissue descriptions, where the tissue was modeled as a network of 1D elements (Dupuy et al, 2006; Hamant et al, 2008; Corson et al, 2009). This allows a reasonable trade-off between modeling expressiveness and computational complexity, but fails at representing efficiently a number of specific properties of higher-dimensional mechanics (Gelder, 1998), such as shear, incompressibility, and anisotropy. To alleviate this difficulty, other authors have adapted the formalism of continuous media to growth (Dumais et al, 2006; Goriely and Amar, 2007; Dyson and Jensen, 2010; Rojas et al, 2011; Fozard et al, 2013; Sassi et al, 2014; Boudon et al, 2015; Bozorg et al, 2016; Hervieux et al, 2016). Boudon *et al.* and Bozorg *et al.* developed a Lockhart-like 2D description of growth using a second-order growth tensor (L_g), expressed as a function of the elastic (reversible) deformation, represented by the elastic strain tensor (E):

$$L_g = \Phi \left(E - \tau I \right)_+ \tag{1}$$

where Φ is the wall extensibility, τ is a threshold strain, $\left(\cdot \right)_+$ is the tensor ramp function (defined in Appendix A) that allows growth only in directions where deformation is higher than the threshold τ; and I is the second-order identity tensor (Boudon et al, 2015; Bozorg et al, 2016). For the sake of simplicity, it is generally assumed that the cell wall extensibility (Φ) is quantified by a scalar coefficient or, equivalently, that growth and strain directions coincide. In the linear elasticity assumption (Hooke's law), strain and stress (depicted by tensor S) are linearly coupled *via* the fourth-order stiffness tensor ($\mathbb{C}_w$):

$$E = \mathbb{C}_w^{-1} : S \tag{2}$$

(':' is the tensor double-dot product). Combining the two previous expressions shows that anisotropic growth results from an anisotropy in stress and/or in stiffness. There is a reduced potential for cells embedded in a tissue, to autonomously regulate their local stress, which is mostly imposed by the rest of the tissue (Boudon et al, 2015). By contrast, by modifying locally the wall's structure, cells can affect growth anisotropy in a more direct manner.

Such a local regulation does occur in plant tissues and has been proposed to rely partly on the activity of cortical microtubules. Microtubules participate in locally structuring the cell wall, by guiding the trajectories of the transmembrane complexes synthesizing the microfibrils (Fig. 1(b), Paredez et al, 2006). There are important indications, that microtubules in many cells align along the main stress

direction (Williamson, 1990; Hamant et al, 2008; Sampathkumar et al, 2014a,b). This has led to the hypothesis that forces, generated in the tissues by turgor and differential growth rates, feed back into the structure of the cell wall *via* microtubule organization.

This so-called *stress feedback* has been integrated into tissue-scale models. Hamant *et al.* used a spring-based cell discretization of the tissue (Hamant et al, 2008). In this approach, stress feedback is taken into account by modulating spring constants according to the angle between the spring and the cells average loading axis. Other authors have instead used a continuous formalism, expressing a coupling between multidimensional stiffness and stress, in Bozorg et al (2014), through triangular biquadratic springs (Delingette, 2008) and in Hervieux et al (2016), through the finite element method (FEM). In the last two implementations, stress is considered as an input-parameter that modulates the main axis of stiffness and its anisotropy.

These studies express an abstract phenomenological link between stress and stiffness, not explicitly taking into account the underlying molecular mechanisms. Here, we describe a modeling approach where subcellular processes involved in the wall synthesis are more explicitly described. Based on a parsimonious kinetic model of microtubule reorganization and microfibril synthesis, we propose a homogenized expression of the walls dynamical elastic properties. We present a general expression of force-induced microtubule stabilization in the direction of higher tension. This simple model leads to subtle predictions on the dynamics of microtubule arrays and gives a quantitative description of wall stiffness. We derive an analytical, quantitative behavior of the microtubule cortex and the material mechanics. Tissue-scale FEM simulations of the system reproduced several macroscale behaviors previously observed *in vivo*.
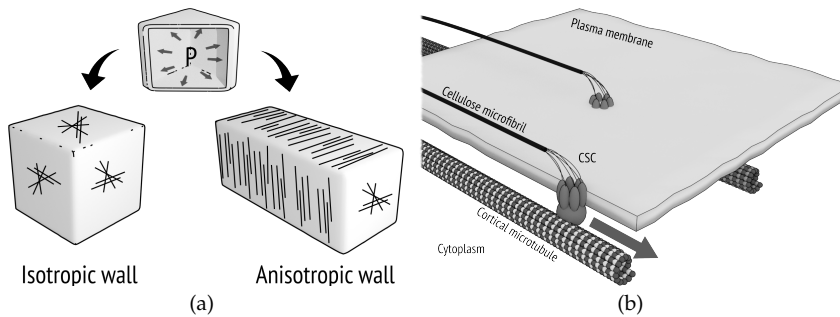

Fig. 1 (**a**) The cell wall as a regulator of growth direction. Schematic of two pressurized cells with different wall properties and same initial shape. The first one has an isotropic wall and display no privileged axis of growth. The other one displays hoop-shaped organization of microfibrils and expands axially. (**b**) Cartoon showing the microtubule-guided transport of cellulose synthase complexes (CSCs). CSCs move along cortical microtubules and across the plasma membrane, and synthesize microfibrils in their wake. Redrawn after Landrein and Hamant (2013).

2 Model

In this section, we introduce our model theoretically, by first detailing the elastic behavior of the wall considered as a fiber-reinforced medium, and then the kinetics of microtubules and microfibrils.

2.1 Mechanical model

2.1.1 Mechanical equilibrium

The meristem is generally assimilated to a thin pressurized shell with uniform thickness (Fig. 2(a), Kutschera, 1991; Beauzamy et al, 2015). This shell defines a continuum on which stiffness, strain and stress can be defined as tensor fields evolving in space and time, respectively $\mathbb{C}_w(x, t)$, $E(x, t)$ and $S(x, t)$ (*NB*, since the next developments are made at a fixed position x, we get rid of the spatial parameter x in the following notations). Due to large radius of curvature (compared to thickness), we assume plane stress within the surface (Landau and Lifshitz, 1986).

Because biological processes occur at a time scale much smaller than elastic relaxation, we assume quasi-static mechanical equilibrium at any time:

$$\forall t \quad \nabla \cdot S(t) + f^P(t) = \mathbf{0} \tag{3}$$

where $\nabla \cdot S$ is the divergence of the tangential stress (inner force at x) and f^P is the pressure force per unit volume applied normally to the surface at x.

2.1.2 Constitutive relation of the material

In higher plants, the wall is mostly composed of three polysaccharides: pectins, hemicelluloses and cellulose (Cosgrove, 2001). The former is polymerized as stiff, linear strands, the microfibrils. They are embedded in a matrix of pectins and hemicelluloses that form an isotropic, soft hydrogel. In addition, other polysaccharides, *e.g.* hemicellulose, as well as numerous enzymes constantly interact and remodel these two main structural elements (Wolf et al, 2012).

In the sequel, it is assumed that this fiber-reinforced hydrogel behaves as a linear deformable solid (Eq. (2)), composed of an isotropic homogeneous matrix and a fiber network (Fig. 2(b)). We assume that fibers are much stiffer than the rest of the material. For that, we neglect the mechanical effect of the possible interaction between the fibers and the matrix. The whole system (*i.e.* fibers + matrix) can thereby be seen as the parallel association of both components. The resulting stiffness tensor $\mathbb{C}_w$ is therefore the sum of the fiber-related $\mathbb{C}_f$ and the matrix $\mathbb{C}_g$:

$$\mathbb{C}_w = \mathbb{C}_g + \mathbb{C}_f. \tag{4}$$

The gel is assimilated to an isotropic deformable solid, described by a Young's modulus and a Poisson's ratio. Tensor $\mathbb{C}_g$ can be expressed in an arbitrary surface basis

(e_x, e_y), by employing the Voigt form[1]:

$$[\mathbb{C}_g] = Y \begin{bmatrix} 1 & \nu & 0 \\ \nu & 1 & 0 \\ 0 & 0 & \frac{1-\nu}{2} \end{bmatrix} \tag{5}$$

where ν and Y respectively stand for the Poisson's ratio and for the reduced Young's modulus[2].

Describing the fiber-related component, which contains the anisotropy of the whole material, requires a mechanical model of the fibers. Those are modeled by linear springs distributed in the surface's tangential plane. For the sake of simplicity, we assume that they do not mutually interact and dot not move relative to the medium[3].

Let $\rho(\theta)$ be the local angular density of fibers[4] in an arbitrary tangential reference frame (e_x, e_y) (Fig. 2(b)). Since mechanically, a fiber is apolar [5], function ρ is π-periodic. As one may expect, the stiffness tensor $\mathbb{C}_f$ is a function of the density ρ. By assuming affine deformation of the fibers (namely that each individual fiber is deformed as the macroscopic medium), one shows that $\mathbb{C}_f$ can be expressed according to the low-frequency Fourier coefficients ρ_0, ρ_1, $\tilde{\rho}_1$, ρ_2 and $\tilde{\rho}_2$ (Appendix B and Cox, 1952):

$$[\mathbb{C}_f] = \frac{\pi Y_f \rho_0}{16} \begin{bmatrix} 3 + \frac{\rho_2 + 4\rho_1}{\rho_0} & 1 - \frac{\rho_2}{\rho_0} & \frac{2\tilde{\rho}_1 + \tilde{\rho}_2}{\rho_0} \\ 1 - \frac{\rho_2}{\rho_0} & 3 + \frac{\rho_2 - 4\rho_1}{\rho_0} & \frac{2\tilde{\rho}_1 - \tilde{\rho}_2}{\rho_0} \\ \frac{2\tilde{\rho}_1 + \tilde{\rho}_2}{\rho_0} & \frac{2\tilde{\rho}_1 - \tilde{\rho}_2}{\rho_0} & 1 - \frac{\rho_2}{\rho_0} \end{bmatrix} \tag{6}$$

where Y_f is the reduced Young's modulus of one fiber.

Assuming that the wall's thickness, the gel's stiffness and Y_f are constant in time, Eqs. (4) to (6) imply that the evolution of the wall's mechanical properties only results from the dynamics of the microfibrils distribution.

2.2 The dynamics of cortical microtubules and microfibrils

The orientation of cellulose deposition depends on the orientation of cortical microtubules that guide the trajectories of transmembrane cellulose synthase complexes (CSCs). In our model, tubulin (namely, the elementary molecular sub-unit of microtubules) is described as a biphasic gel: it can be found either in a monomeric soluble state or in a polymerized form (the microtubule). The distribution of microtubules is described through its π-periodic angular distribution ϕ.

In our model, microtubule orientation influences only the orientation of cellulose deposition, and has no impact on the mass of cellulose polymerized per unit

---

[1] Due to the symmetries $\mathbb{C}_{ijkl} = \mathbb{C}_{klij}$ and $\mathbb{C}_{ijkl} = \mathbb{C}_{ijlk} = \mathbb{C}_{jikl} = \mathbb{C}_{jilk}$, a given stiffness tensor $\mathbb{C}$ can be expressed as a 3×3 matrix (Voigt notation).

[2] The actual Young's modulus divided by $1 - \nu^2$.

[3] In reality, fibers are connected through the hemicellulose network, that is yet assumed to be significantly softer than the fibers and then negligible.

[4] For given positions x and angle θ (angle with e_x in the tangential plane), $\rho(\theta) \, d\theta$ is the number of fibers at the vicinity of x whose orientation angle lies in the infinitesimal interval $[\theta, \theta + d\theta]$.

[5] A fiber can be modeled by a straight line, equivalently defined by the unit vectors $e_\theta = \cos\theta e_x + \sin\theta e_y$ or $-e_\theta$.
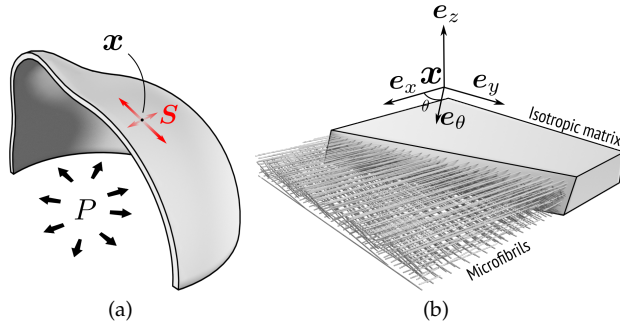
Fig. 2 Mechanical model of the epidermis. (**a**) The tissue is represented by a pressure-filled thin membrane. (**b**) Sketch of the wall structural model: microfibrils are immersed in an elastic solid isotropic hydrogel.

time. In brief, this relies on the hypothesis that a CSC protein participates to cellulose deposition regardless of whether it is bound to a microtubule (Emons et al, 2007), as detailed in Appendix C. Hence, cellulose polymerization is expressed as a function of the *normalized* microtubule distribution $\phi^* = \phi / \int_\pi \phi$. In addition to that polymerization term, we introduce an isotropic decay that prevents unlimited accumulation of cellulose in the wall. At the considered time scale, we neglect growth, and then, the microfibril advection that it would induce. Finally, we express the evolution of the angular density of microfibrils as:

$$\mathrm{d}_t \rho\left(\theta, t\right) = k_\rho \phi^*\left(\theta, t\right) - k_\rho' \rho\left(\theta, t\right),\tag{7}$$

(k_ρ and k_ρ' are kinetic constants).

The evolution of the microtubule angular density ϕ emerges from a description of the tubulin polymerization/depolymerization kinetics. Tubulin is present in the cytoplasm under two forms: a soluble one composed of free dimers (with concentration c_{free}), and a polymerized one depicted by ϕ. We assume that its total concentration c_0 (namely regardless of its form) is constant and uniform. This concentration verifies:

$$c_0 = c_{\mathrm{free}} + \int_\pi \phi.\tag{8}$$

Microtubule dynamics is governed by the conservation equation of tubulin:

$$\mathrm{d}_t \phi\left(\theta, t\right) = k_\phi c_{\mathrm{free}} - k_\phi'\left(\mathbf{S}, \theta\right) \phi\left(\theta, t\right).\tag{9}$$

The synthesis term (first term on the right-hand side) describes the isotropic microtubule nucleation from the pool of free dimers (with kinetic constant k_ϕ). The second term models the microtubule depolymerization rate. Unlike in Eq. (7), the microtubule depolymerization rate varies with the orientation according to the angular function $k_\phi'\left(\mathbf{S}, \theta\right)$, that models stress sensing. The last is described by assuming that microtubule stability increases with the tensile stress angular distribution f, reducing the degradation probability according to:

$$k_\phi'\left(\mathbf{S}, \theta\right) = k_\phi'^0 e^{-\gamma f\left(\mathbf{S}, \theta\right)},\tag{10}$$

where k'^{0}_{ϕ} stands for the inverse half-life of polymerized tubulin in absence of stress, γ is a (positive) coupling parameter, and $f(S, \theta) = e_{\theta} \cdot S \cdot e_{\theta}$ depicts the force per unit surface in direction θ (details on the establishment of Eq. (10) are provided in Appendix D). This angular variability of the microtubule depolymerization probability over the local orientation of the stress field is the key feature of our modeling approach and accounts for the experimentally-observed tendency of microtubules to align in the direction of maximal tension (Hamant et al, 2008). The general hypothesis behind this is that microtubules under tension undergo some conformational change making them less sensitive to katanin severing activity and therefore increasing their lifetime (Landrein and Hamant, 2013; Sampathkumar et al, 2014a).

In the last two sections, we established a dynamical model of the wall's stiffness, by describing (i) the relation between the stiffness tensor $\mathbb{C}_w$ and the microfibril bundle (Eqs. (4) to (6)), (ii) the microtubule-guided deposition of microfibrils (Eq. (7)) and (iii) the stress-regulated kinetics of microtubules (Eqs. (8) to (10)). Importantly, Eqs. (4) to (7) and (11) can be conceptually combined into a single ordinary differential equation relating the time evolution of the stiffness tensor $\mathbb{C}_w$ to stress.

2.3 Tissue-scale numerical simulation procedure

Our model expresses the *local* behavior of the system, focusing on an infinitesimal portion of tissue in which stress is an exogenous parameter. We extended the analysis to a large-scale tissue, represented as an elastic surface, loaded with constant pressure (Fig. 2(a)). In this context, stress results from curvature and pressure; and may evolve in time as the stiffness properties vary.

Due to its nonuniform curvature, the tissue experiences nonuniform stress field. In practice, the stress and the elastic response of such a system (its displacement field) can generally only be determined by numerical approximation.

For that, we employed FEM (in space) with triangle meshes, coupled with a *finite difference* time discretization. At initial time $t = t_0$, the microtubule/microfibril system is considered at equilibrium (null-stress steady state, isotropic distribution, see Eq. (30)). The structures are not loaded and no residual stress is assumed.

Assuming that the microtubules' transient regime is much shorter than that of cellulose deposition, microtubule distribution can be considered at equilibrium, which is described by the steady-state solution of Eq. (9):

$$\phi^{\infty}(S, \theta) = \frac{c_0 K_{\phi} e^{\gamma f(S, \theta)}}{1 + K_{\phi} \int_{\pi} d\theta' e^{\gamma f(S, \theta')}},$$
(11)

with $K_{\phi} = k_{\phi}/k'^{0}_{\phi}$, the equilibrium constant of the microtubule stress-free polymerization process.

Under this assumption, only the microfibril distribution can vary. It is iteratively updated, on each finite element, by considering the steady-state microtubule distribution (Eq. (11)), and the microfibril evolution equation (Eq. (7)) solved through Euler's method (Eq. (29)). After this step, stiffness is updated according to Eq. (6), bringing the system out of equilibrium and providing an new initial state. For further details on the numerical pipeline, refer to Appendix F.

3 Results

We detail hereafter the outputs of the model exposed in the previous section. We first expose how the microtubule steady state accounts for the experienced stress field. We then show how the cell wall equivalent stiffness tensor is modified and how that leads to nontrivial strain response.

3.1 The steady microtubule/microfibril pattern reflects stress

This section exposes results on the steady-regime behavior derived from Eqs. (4) to (7) and (11) (refer to Appendix E for detailed mathematical developments).

The steady-state expression of the microtubule distribution ϕ^∞ (Eq. (11)) expresses their tendency to crowd in the direction of largest tensile stress (Fig. 3(a)). Quantification of the microtubule coalignment has been proposed by Boudaoud et al (2014), based on the concept of *nematic tensor* (see Section F.3). The authors define *microtubule anisotropy* as the ratio:

$$\alpha_\phi^\infty = \frac{Q_{\phi,1}^\infty - Q_{\phi,2}^\infty}{Q_{\phi,1}^\infty + Q_{\phi,2}^\infty} \in [0,1] \tag{12}$$

where $Q_{\phi,1}^\infty \geq Q_{\phi,2}^\infty \geq 0$ are the eigenvalues of the microtubule nematic tensor. This definition of anisotropy can be expressed in the Fourier formalism, as it is equivalent to:

$$\alpha_\phi^\infty = \frac{|\hat{\phi}_1^\infty|}{\hat{\phi}_0^\infty} \left(= \frac{\sqrt{\phi_1^2 + \tilde{\phi}_1^2}}{\phi_0} \right) \tag{13}$$

where $\{\hat{\phi}_n^\infty\}_{n\in\mathbb{N}}$ depicts the Fourier sequence of ϕ^∞ (see Section F.3 for a proof). Similarly, the anisotropy of stress can be defined as $\alpha_f = (S_1 - S_2)/(S_1 + S_2)$ (where $S_1 \geq S_2$ are the stress eigenvalues)[6]. Again, by developing the expression $f(\boldsymbol{S}, \theta) = \boldsymbol{e}_\theta \cdot \boldsymbol{S} \cdot \boldsymbol{e}_\theta$, one shows that $\alpha_f = 2|\hat{f}_1|/\hat{f}_0 \, (= 2\sqrt{f_1^2 + \tilde{f}_1^2}/f_0)$.

As shown in Figs. 3(a) and 3(b), and Eq. (26), α_ϕ^∞ is a growing function of the stress anisotropy, but also of the mean stress $f_0 = \text{Tr}(\boldsymbol{S})/2$. Similarly, the concentration of microtubules ($\pi\phi_0^\infty/2$) is a growing function of stress anisotropy and amplitude (Fig. 3(c) and Eq. (25)). Note that if high stress amplitude favors high microtubule coalignment, we can expect that this effect also comes with a lengthening of the transient regime's duration, due to the augmented stability of microtubules that diminishes microtubule turnover [7].

Considering infinitesimal displacements, one can assume that the global shape, and therefore the distribution of the pressure forces, do not vary during the evolution of the material stiffness. This allows to derive the steady-state microfibril distribution from Eq. (11):

$$\rho^\infty(\boldsymbol{S}, \theta) = K_\rho \phi^{*\infty}(\boldsymbol{S}, \theta) = \frac{K_\rho e^{\gamma f(\boldsymbol{S},\theta)}}{\int_\pi \mathrm{d}\theta' e^{\gamma f(\boldsymbol{S},\theta')}}. \tag{14}$$

---

[6] Note that this definition makes sense only for tensile stress ($S_1 \geq S_2 \geq 0$).

[7] This can be mathematically intuited by additionally assuming that $c_0 \gg \int_\pi \phi$, which reduces Eq. (9) to a linear ordinary differential equation. Its solution displays an initial slope ($|\mathrm{d}_t\phi(\theta, t_0)|$) proportional to $k'_\phi(\boldsymbol{S}, \theta)$ (that is a decreasing function of f_0).

The anisotropy of the microfibril steady distribution, defined as $\alpha_\rho^\infty = |\hat{\rho}_1^\infty|/\hat{\rho}_0^\infty$, is equal to that of microtubules (α_ϕ^∞), but its concentration does not depend on stress (due to the normalization of ϕ in Eq. (7)). The microfibril steady distribution is also independent of the microtubule chemical kinetics.

(a) Microtubule distribution

(b) Microtubule anisotropy

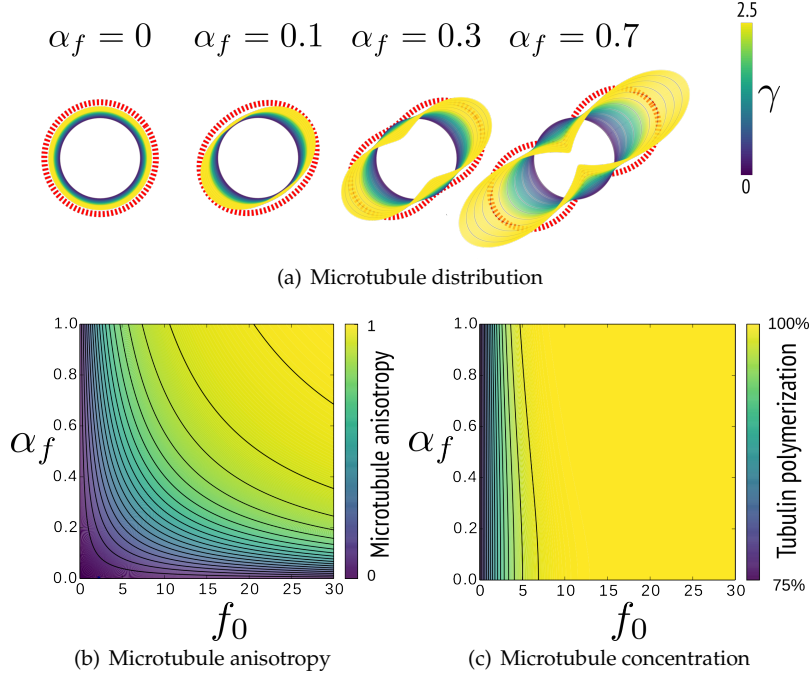(c) Microtubule concentration

Fig. 3 Steady state of the microtubule distribution. Microtubules respond nonlinearly to stress anisotropy *and* amplitude. Microtubule anisotropy depends equally on both stress anisotropy and amplitude. (**a**) Visualization of the microtubule distribution ϕ according to the stress anisotropy α_f ($f_0 = 1$ MPa) and the coupling coefficient γ. The red dashed line represents the polar distribution of forces f. (**b**) Anisotropy α_ϕ^∞ of the microtubule distribution as a function of f_0 (expressed in MPa) and stress anisotropy α_f with stress feedback. (**c**) Relative concentration of polymerized tubulin $c_P^\infty/c_0 = \pi/2\phi_0^\infty/c_0$ as a function of f_0 (expressed in MPa) and stress anisotropy α_f with stress feedback. Parameters for (**b-c**): $c_0 = 1$ mol.μm^{-3}, $\gamma = 10^{-6}$Pa^{-1}, $K_\phi = 1$.

3.2 The effect of stress feedback on elastic deformation

Under the previous assumption that stress does not vary much as stiffness evolves in time, the steady-regime stiffness tensor $\mathbb{C}_w^\infty$ is an explicit function of the microtubule distribution (Eqs. (4) to (7), (14) and (25)). In particular, one can choose (without loss of generality) the surface basis such that e_x coincides with the main eigenvector of stress. In this basis, the microfibril distribution ρ^∞ is even (its odd Fourier

coefficients $\{\tilde{\phi}_n^{\infty}\}_{n \in \mathbb{N}}$ vanish) and $\left[\mathbb{C}_f^{\infty}\right]$ becomes:

$$\left[\mathbb{C}_f^{\infty}\right] = \frac{K_{\rho} Y_f}{8} \begin{bmatrix} 3 + 4\alpha_{\phi}^{\infty} + \beta_{\phi}^{\infty} & 1 - \beta_{\phi}^{\infty} & 0 \\ 1 - \beta_{\phi}^{\infty} & 3 - 4\alpha_{\phi}^{\infty} + \beta_{\phi}^{\infty} & 0 \\ 0 & 0 & 1 - \beta_{\phi}^{\infty} \end{bmatrix} \tag{15}$$

where $\beta_{\phi}^{\infty} = |\hat{\phi}_2^{\infty}|/\hat{\phi}_0^{\infty}$ and $K_{\rho} = k_{\rho}/k_{\rho}'$ is the isotropic-stress equilibrium constant of cellulose deposition. By combining the previous equation with the expression of the Fourier coefficients of ϕ (Eq. (25)), tensor $\mathbb{C}_w^{\infty} = \mathbb{C}_f^{\infty} + \mathbb{C}_g$ can be written as a function of stress, yielding the stress/strain nonlinear relationship illustrated in Fig. 4(a). Eq. (15) states that the material is asymptotically more resistant to traction in the direction of main stress ($\mathbb{C}_{w,11}^{\infty} \geq \mathbb{C}_{w,22}^{\infty}$). Moreover, it is orthotropic (symmetric) according to the stress axes ($\mathbb{C}_{w,13}^{\infty} = \mathbb{C}_{w,23}^{\infty} = 0$)[8]. This is due to the asymmetry of the microfibril distribution, due to a transient phase shift between the respective distributions of microtubules and microfibrils, representing the inertia of the system.

In anisotropic elasticity, the respective directions of maximal stress and strain are in general different. In our specific case though, at steady-state, the orthotropy of the stiffness tensor in the stress eigenbasis imposes that both fields (stress and strain) share the same eigenvectors. An alternative remains: either directions of maximal (and minimal) eigenvalues of both fields are parallel or orthogonal. Those two regimes were notably characterized in Bozorg et al (2014) according to the anisotropy of the material's stiffness. We show how the orthogonality between the main directions of stress and strain can be expressed as a condition on stress only, using the dependence of stiffness on stress. By comparing the ratio

$$\frac{E_{\perp}^{\infty}}{E_{\parallel}^{\infty}} = \frac{S_2 \mathbb{C}_{w,11}^{\infty} - S_1 \mathbb{C}_{w,12}^{\infty}}{S_1 \mathbb{C}_{w,22}^{\infty} - S_2 \mathbb{C}_{w,12}^{\infty}}$$

(obtained by inverting Eq. (2), and illustrated in Fig. 4(c)) between longitudinal strain $E_{\parallel}^{\infty}$ (collinear to main stress) and orthogonal strain $E_{\perp}^{\infty}$ (orthogonal to main stress), to 1, a necessary and sufficient condition for orthogonality can be derived:

$$\alpha_f < \frac{\mathbb{C}_{w,11}^{\infty} - \mathbb{C}_{w,22}^{\infty}}{\mathbb{C}_{w,11}^{\infty} + \mathbb{C}_{w,22}^{\infty} + 2\mathbb{C}_{w,12}^{\infty}}.$$

By expressing matrix coefficients $\mathbb{C}_{w,ij}^{\infty}$ according to Eq. (4), (5) and (15), the previous condition becomes:

$$\alpha_f < \frac{\alpha_{\phi}^{\infty}}{1 + 2\eta} \quad \text{with} \quad \eta = \frac{(1 + \nu) Y}{K_{\rho} Y_f}, \tag{16}$$

where η measures the relative stiffness between the gel and the fiber components; the quantity $\alpha_{\phi}^{\infty} (1 + 2\eta)^{-1}$ is a measure of the material's anisotropy. This *strain orthogonalization* directly relies on the sharpness of the microtubule alignment, and therefore on the stress field (Eqs. (11) and (26) and Fig. 4(c)). Note that since the anisotropy ratio α_{ϕ}^{∞} lies in $[0, 1]$, strain orthogonalization cannot occur for excessive

---

[8] In the transient regime however, orthotropy cannot be assumed, since the choice of the reference axis does not eliminate both $\tilde{\rho}_1$ and $\tilde{\rho}_2$ in general.

stress anisotropy. In fact, Ineq. (16) cannot be verified if $\alpha_f \geq (1 + 2\eta)^{-1}$; this limitation comes from the residual isotropy due to the isotropic component (Eq. (4)). In brief, we have shown how two mechanical regimes (orthogonality or collinearity of the stress and strain main directions) can be explicitly accounted for by the chemical properties of the microtubule array (notably through the sensitivity parameter γ). In particular, *strain orthogonalization* cannot occur if microtubules are less anisotropic than stress (Ineq. (16)).

Although the number of microfibrils, regardless of their orientation, does not depend on stress, we observe differences in the material's areal dilation between the stress-responsive ($\gamma > 0$) and isotropic ($\gamma = 0$) materials. This difference is a general property of fibrous materials, for which areal dilation varies with material anisotropy. Fig. 4(b) illustrates the emergence of this effect from stress directly. It allows identifying a particular domain where stress feedback produces higher dilation than in the case of an isotropic, non stress-sensing material. In a biological context, that implies that anisotropic-walled cells could expand faster than isotropic ones, all other parameters being equal. In addition, due to the non-linearity in the strain-based growth equation (Eq. (1)), an anisotropic cell may experience one-directional growth, whilst its isotropic counterpart could be kept under the strain threshold in all directions, preventing its irreversible expansion.

3.3 Effect of *strain orthogonalization* on tissue-scale development

In order to characterize the impact of the feedback process on an entire structure, we compare the strain field of an inert (non-responsive) material ($\gamma = 0$) and a stress-responsive material ($\gamma > 0$), at steady regime. In fact, Eq. (1) formulated in Boudon et al (2015); Bozorg et al (2016) expresses the local growth rate as a piecewise linear function of the strain, suggesting that the elastic response of the tissue directly allows computing its immediate growth. In our context, where no growth is considered, we infer qualitative properties of growth from elastic strain.

One of the simplest shapes, involving anisotropic stresses, is the cylinder. Similar geometries have been studied in the context of plant modeling as they can be considered as idealized stems (Hamant et al, 2008; Bozorg et al, 2014; Sassi et al, 2014; Boudon et al, 2015). We employ here a cylinder closed by a hemispherical cap and fixed at its boundary (Fig. 5). In this case, stress is known from continuous mechanics: it is anisotropic in the cylindrical trunk where hoop stress S_1 equals twice axial stress S_2, and isotropic on the cap (mean stress is equal to S_2), as confirmed by FEM (Fig. 5(a) and 5(b)).

In absence of feedback ($\gamma = 0$, then microtubule distribution is isotropic, Fig. 5(c)), circumferential stress results in circumferential strain (Fig. 5(e)) that should tend to break the cylindrical shape. By activating the feedback process ($\gamma > 0$), microtubules align in a circumferential way on the trunk, and is isotropic on the cap (Fig. 5(d)).

Enabling the feedback ($\gamma > 0$) may allow strain to become maximal in the axial direction (orthogonal to stress), provided a value of γ satisfying Ineq. (16) (Figs. 5(f) and 5(b)). This results in a slimming and an axial stretching of the cylindrical trunk.

One also observes that the dilation of the finite elements (areal expansion, equal to $\mathrm{Tr}(E)$ for small deformation) is bigger with the feedback than without (Figs. 5(e) and 5(f)), corresponding to the positive domain in Fig. 4(b).

(a) Areal dilation without and with stress feedback

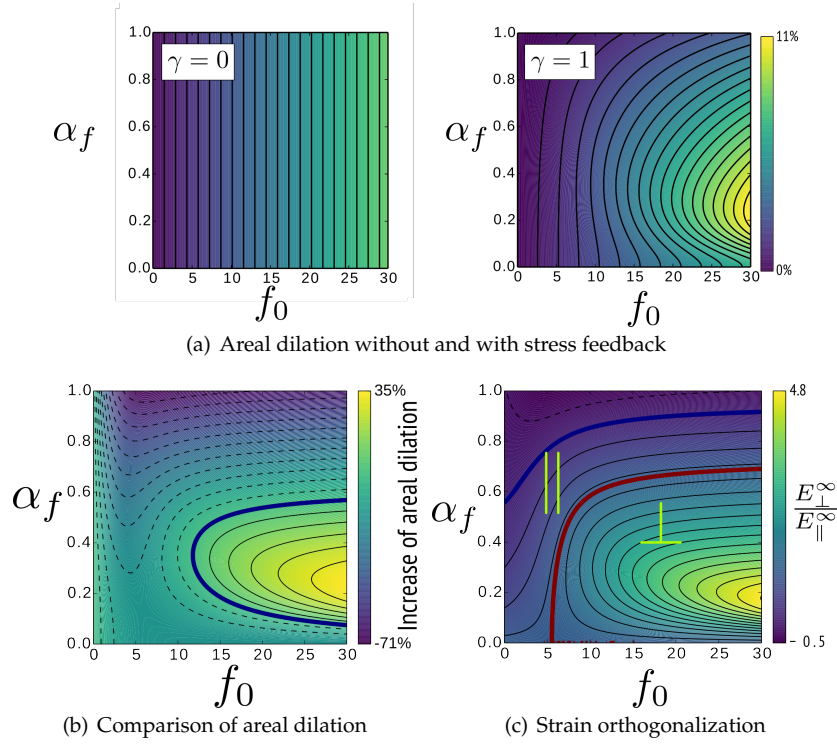(b) Comparison of areal dilation

(c) Strain orthogonalization

Fig. 4 The effect of stress feedback on elastic strain. Stress feedback confers nonlinear elastic properties to the material. Two noticeable effects are the effect of microfibril reorganization on areal expansion (that may differ relative to the isotropic linear case) and the strain and stress respective directions (that may be orthogonal). (**a**) Areal dilation ($\mathrm{Tr}(E^\infty)$) Δ_{OFF} without ($\gamma = 0$) and Δ_{ON} with ($\gamma = 1$, unit: 10^{-6} Pa^{-1}) feedback. In absence of feedback, dilation is a linear function of f_0, which is not the case with feedback. (**b**) Relative variation $(\Delta_{\mathrm{ON}} - \Delta_{\mathrm{OFF}})/\Delta_{\mathrm{OFF}}$ (in %) of areal dilation between a stress-responsive material ($\gamma = 1$) and a non-responsive material ($\gamma = 0$), as a function of f_0 (expressed in MPa) and stress anisotropy α_f. Blue bold contour indicates level 0 ($\Delta_{\mathrm{OFF}} = \Delta_{\mathrm{ON}}$). (**c**) Ratio $E_\perp^\infty / E_\parallel^\infty$ of strain (in the stress eigenbasis, where the basis vectors are sorted according to the descending order of eigenvalues) as a function of f_0 (expressed in MPa) and α_f, with stress feedback. Main stress and strain are orthogonal *iff* $E_\perp^\infty / E_\parallel^\infty > 1$; domains labeled $\perp$ and $\parallel$ respectively indicate those where main stress and strain are orthogonal or collinear. Blue and red bold contours respectively indicate levels 0 (null orthogonal strain $E_\perp^\infty$) and 1 (isotropic strain $E_\perp^\infty = E_\parallel^\infty$). Parameters: c_0 (arbitrary), $\gamma = 10^{-6}$ Pa^{-1}, $K_\phi = 1$ (arbitrary), $K_\rho = 1$ mol.μm^{-3}, $Y_{\mathrm{f}} = 2$ GPa, $\nu = 0.2$, $Y = 0.2$ GPa.

The previous simulation involves a positively curved shape. Yet, plants, and in particular the meristem, display several negatively curved zones (for example at the frontier between organs). This scenario has been idealized by merging two sphere meshes, creating a negatively curved junction (Fig. 6).

In that case, the outgrowth generates a high circumferential stress at the concave bend between the two spheres, where the gaussian curvature is negative (Figs. 6(b) and 6(c)). Consequently, the strain field is also highly circumferential in absence of feedback (Fig. 6(f)). This contributes to augment the size of the frontier, relative to the reference state.
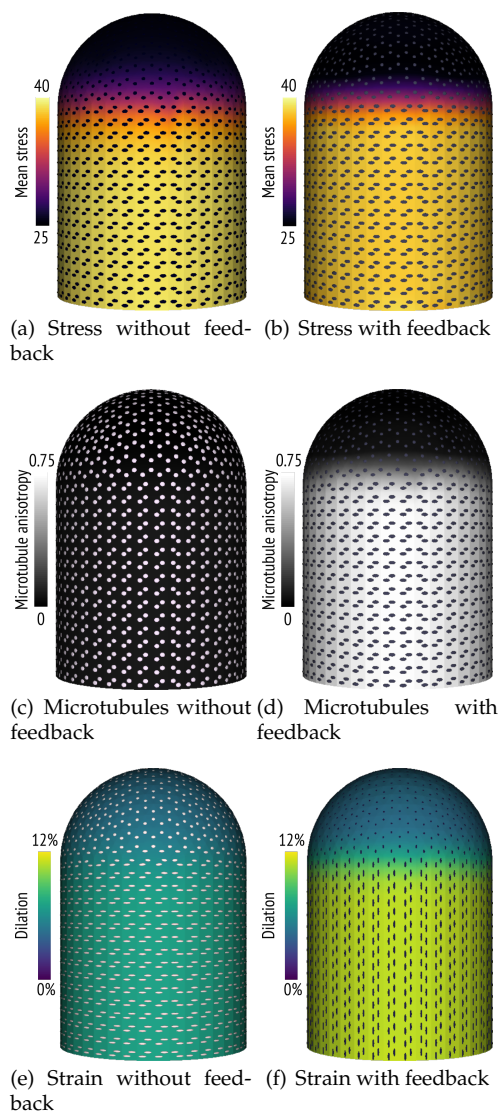
(a) Stress without feedback (b) Stress with feedback

(c) Microtubules without feedback (d) Microtubules with feedback

(e) Strain without feedback (f) Strain with feedback

Fig. 5 Virtual stem. Circumferential hoop stresses promote circumferential coalignement of microtubules resulting in axial elongation. (**a-b**) Stress field. Heat map: mean stress $f_0/2$ (in MPa), elliptic representation of the tensor. (**a**) In absence of feedback, (**b**) with feedback. (**c-d**) Microtubule distribution. Heat map: microtubule anisotropy α_ϕ^∞, ellipses: alignment tensor (see Appendix F). (**c**) In absence of feedback, (**d**) with feedback. (**e-f**) Strain field. Heat map: dilation $\mathrm{Tr}(\boldsymbol{E})$. (**e**) In absence of feedback, (**f**) with feedback. Parameters: stem dimensions 300 μm × 200 μm, turgor pressure $P = 0.5$ MPa, c_0 (arbitrary), $\gamma = 2 \times 10^{-7}$ Pa^{-1}, $K_\phi = 1$, $K_\rho = 1$ mol.μm^{-3}, $Y_\mathrm{f} = 20$ GPa, $\nu = 0.2$, $Y = 1$ GPa.

In contrast, the stress feedback allows to compensate for the circumferential stress, and develop axial strains (Figs. 6(c) and 6(g)). In this case, the decrease of the circumferential strain contributes to maintaining the size of the frontier, reinforcing

the separation between the meristem and its primordia, for instance. This example reinforces the idea exposed in Bozorg et al (2014), that the feedback promotes the anisotropy of shape, preserving non-spherical curvature.
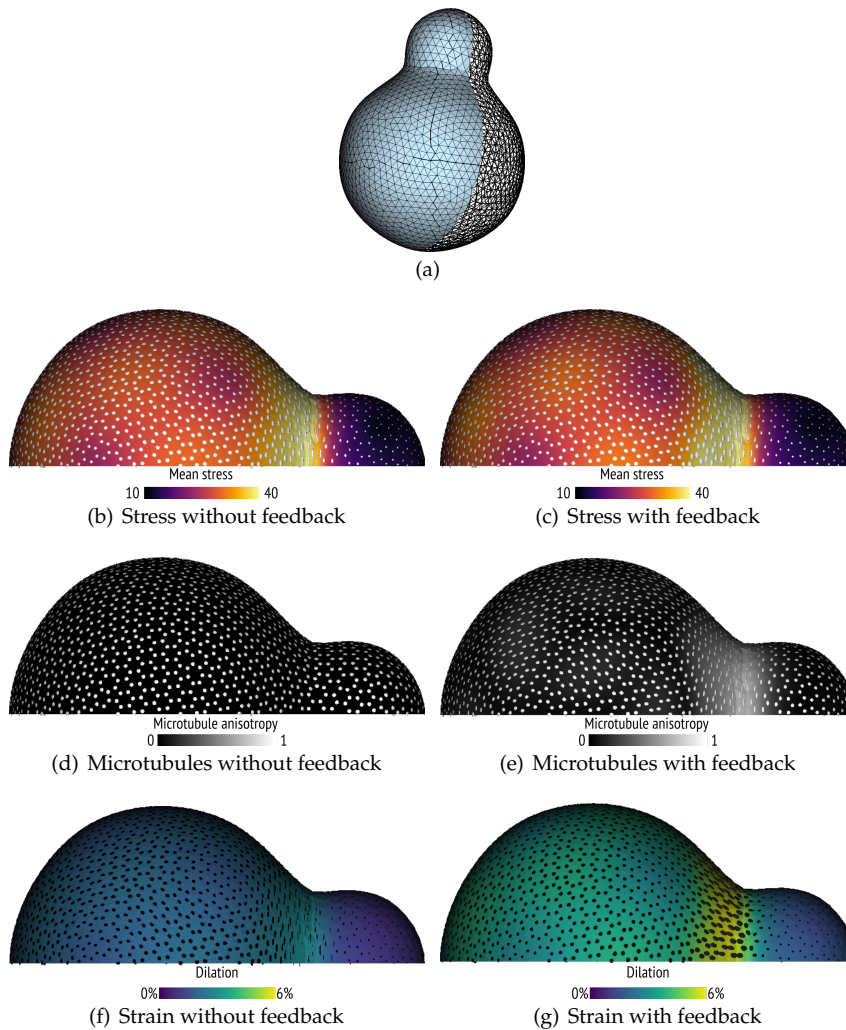

Fig. 6 Virtual outgrowing organ. Highly anisotropic stresses at the concave frontier contribute to maintain the latter that expands mainly axially. (**a**) Original mesh and visualized cut (in blue). (**b-c**) Stress field. Heat map: mean stress $f_0/2$ (in MPa), elliptic representation of the tensor. (**b**) In absence of feedback, (**c**) with feedback. (**d-e**) Microtubule distribution. Heat map: microtubule anisotropy α_ϕ^∞, ellipses: alignment tensor (see Appendix F). (**d**) In absence of feedback, (**e**) with feedback. (**f-g**) Strain field. Heat map: dilation $\mathrm{Tr}(\boldsymbol{E})$. (**f**) In absence of feedback, (**g**) with feedback. Parameters: mesh characteristic dimension 100 μm (order of magnitude), turgor pressure $P = 0.5$ MPa, c_0 (arbitrary), $\gamma = 10^{-6}$ Pa^{-1}, $K_\phi = 1$, $K_\rho = 1$ mol.μm^{-3}, $Y_\mathrm{f} = 20$ GPa, $\nu = 0.2$, $Y = 0.3$ GPa.

As a supplemental layer of shape complexity, the effect of a topological change has been examined. We represented this scenario through a circular hole in a hemispherical cap (fixed at its boundary), mimicking the ablation experiments described in Hamant et al (2008); Sampathkumar et al (2014a).

Here, highly anisotropic stresses are generated at the hole's vicinity (Figs. 7(b) and 7(c)). In absence of feedback, this would promote an expansion of the hole (Fig. 7(f)). With feedback, the steady-regime strain features radial orientation (Fig. 7(g)) or, at least, less anisotropic circumferential orientation (where strain orthogonalization fails, see Eq. (16)), allowing a decrease of the hole's circumference relative to the non-stress-sensing case. This comes with a relaxation of the circumferential stress amplitude (around 10% with the present parameters) at the close periphery of the hole (Figs. 7(b) and 7(c)). To sum this up, it seems that a strain-based growth, coupled with a stress feedback may tend to close topological defects such as holes.

4 Discussion

Existing modeling efforts assessing the feedback mechanism between mechanics and growth in plant tissues rely on a phenomenological *black box* to express the influence of stress on cell wall stiffness (Hamant et al, 2008; Bozorg et al, 2014; Hervieux et al, 2016). This work is an effort to open this black box by making a first step toward a more quantitative, mechanistic, multiscale analysis of stress-based feedback. This approach relies on a parsimonious description of the chemical behavior of cortical microtubules, coupled to cellulose microfibril deposition. A homogenization procedure allows us to derive from the angular distribution of these microfibrils a continuous expression of stiffness as a function of its low-frequency Fourier coefficients, as described in Cox (1952). In this formalization, the material stiffening in the direction of main tension results from the anisotropization of the microtubule array due to the stress field. The coupling between a linear constitutive relation (Hookes law, Eq. (2)) and a nonlinear dependency of the elastic properties upon stress yields an integrated formulation of the behavior, in which stiffness is expressed as a function of stress itself:

$$E^{\infty} = \mathbb{C}_{\mathrm{w}}^{\infty} \left(S \right)^{-1} : S.$$

This expression captures the nonlinear behavior of the wall depicted in Figs. 3 and 4.

Although growth is not included, the model can be useful in exploring the role of a stress-based feedback on growth. Indeed, assuming that growth is a piece-wise linear function of strain (Eq. (1), Boudon et al, 2015; Bozorg et al, 2016), the predicted strain patterns can be used as a proxy for the immediate growth.

In a situation where elasticity is isotropic or slightly anisotropic, strain and stress share the same main axis. Our FE simulations suggest that in that case strain-based growth should favor spherical shapes, while cylinders or more complex shapes cannot be obtained (see also Bozorg et al, 2014). Indeed, these shapes require that the main strain and stress directions are orthogonal. This is possible only if the elastic anisotropy of the material is higher than the stress anisotropy (Ineq. (16)). *In vivo*, expansion can occur in parallel or perpendicular to the maximal stress direction, depending on the type of tissue (Burian et al, 2013). Our model captures
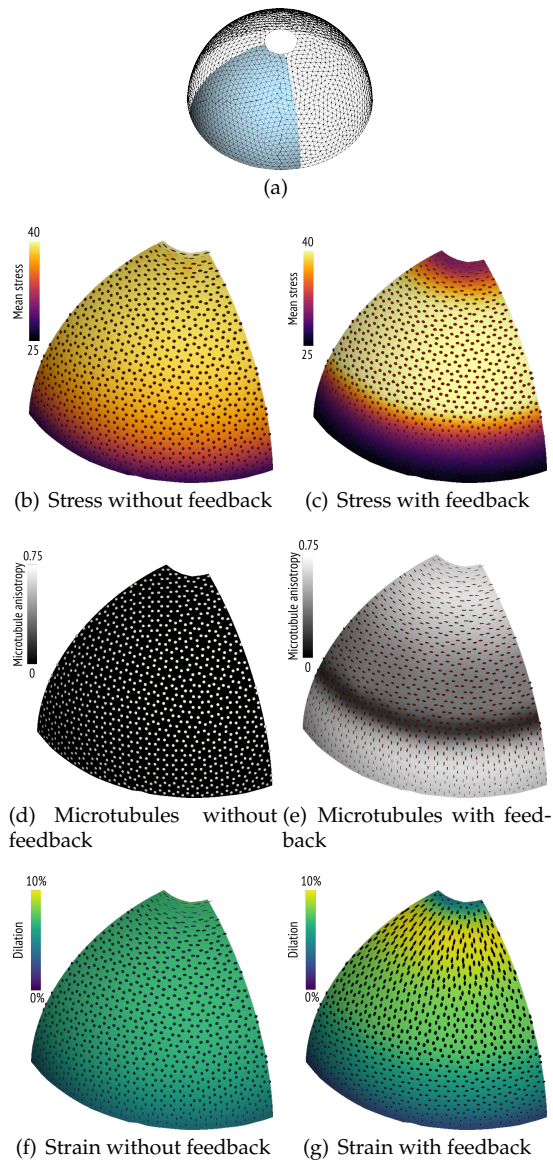
(a)

(b) Stress without feedback   (c) Stress with feedback

(d) Microtubules without feedback   (e) Microtubules with feedback

(f) Strain without feedback   (g) Strain with feedback

Fig. 7 Holed cap. Circular reorganization of microtubules allows to limit the effect of the breach by promoting radial expansion around the hole. (**a**) Original mesh and visualized cut (in blue). (**b-c**) Stress field. Heat map: mean stress $f_0/2$ (in MPa), elliptic representation of the tensor. (**b**) In absence of feedback, (**c**) with feedback. (**d-e**) Microtubule distribution. Heat map: microtubule anisotropy α_ϕ^∞, ellipses: alignment tensor (see Appendix F). (**d**) In absence of feedback, (**e**) with feedback. (**f-g**) Strain field. Heat map: dilation $\mathrm{Tr}(\boldsymbol{E})$. (**f**) In absence of feedback, (**g**) with feedback. Parameters: mesh characteristic dimension 100 μm (order of magnitude), turgor pressure $P = 0.5$ MPa, $\gamma = 2 \times 10^{-7}$ Pa^{-1}, c_0 (arbitrary), $K_\phi = 1$, $K_\rho = 1$ mol.μm^{-3}, $Y_{\mathrm{f}} = 20$ GPa, $\nu = 0.2$, $Y = 0.5$ GPa.

this complexity thanks to the exponential form of the microtubule degradation rate (Eq. (10)). Indeed, this superlinear amplification of the differential of force in the microtubule distribution (Fig. 3(a)), allows the system to satisfy the *strain orthogonalization* condition (Ineq. (16)) in specific cases, such as along an axis or around a hole or a bump. Fig. 4(c) shows that orthogonalization may happen, provided a sufficient stress amplitude f_0, but fails with excessive stress anisotropy (Ineq. (16), Fig. 4(c)) due to the presence of an isotropic matrix. The regulation of the matrix through the dimensionless ratio η, should affect the mean stiffness and anisotropy of the material. Such a regulation, *e.g.* occurring through auxin-induced alteration of the pectin gel, has been experimentally reported (Peaucelle et al, 2011; Braybrook and Peaucelle, 2013).

Based on the strain orthogonalization condition (Ineq. (16)), our model allows to make predictions on the growth behavior in different biological scenarios. In the case of wound-induced stress, idealized in our simulations conducted on a punctured dome (Fig. 5, Hamant et al, 2008; Sampathkumar et al, 2014a), stiffening in the circumferential direction leads to maximal strain in the radial direction. Supposedly, this could enhance the efficiency of a wound healing process based on strain-based growth.

Similarly, our simulations predict that a bulging primordium generates a highly anisotropic stress pattern around itself. This, in turn, should sharply amplify growth heterogeneity between the outgrowth and its surroundings (Fig. 6). More generally, in the previously studied scenarios, stress feedback tends to modify the strain field, counteracting the natural tendency of pressure to induce a spherical shape, preserving the negative curvature at the periphery of an organ or promoting axial expansion (Fig. 5).

In addition, our model includes crucial molecular processes underlying the control of wall mechanics. The degradation term expressed by Eq. (10) can, *in vivo*, be related to *katanin*-based microtubule severing. Katanin is a major regulator of microtubule dynamics in both plants and animals and is involved in the formation of anisotropic microtubular arrays (Burk and Ye, 2002). Although the precise mechanism is not understood, it facilitates microtubule ordering along the main stress direction (Uyttewaal et al, 2012). At a molecular scale, the stabilization of microtubules by stress can be related to possible stress-induced conformational changes undergone by tubulin (Landrein and Hamant, 2013; Sampathkumar et al, 2014a), analogous to those occurring in animal cortical biopolymers (Ghanti et al, 2016). In the context of an anisotropic stress field, the tensile forces exerted on microtubules and, therefore, the efficiency of the katanin activity vary from one direction to another. We modeled this molecular mechanism as a stress-dependent expression of the microtubule depolymerization rate (Eq. (10)). This expression, inspired by studies on other force-sensitive biomolecular systems (Bell, 1978; Nicolas et al, 2004; Changeux, 2012), depicts the idea that the force-induced conformational change of microtubules modifies the enthalpy of the katanin-microtubule reaction. More specifically, its activation barrier is increased by the work of tensile forces exerted on microtubules, leading to their stabilization. The resulting exponential dependency of the degradation rate on tensile force enables the amplification of the microtubule response to mechanical loading. For the sake of simplicity, we neglected interactions between microtubules in the dynamics described by Eq. (9). In a finer model, those should be integrated as well, for they support the capacity of self-alignment

of microtubule arrays (Dixit and Cyr, 2004; Allard et al, 2010; Tindemans et al, 2010) and could enhance the stress-sensitive mechanism we describe here.

Experimental tools to quantify microtubule distributions in plant tissues have been developed recently (Boudaoud et al, 2014; Tsugawa et al, 2016). Combining these measurement techniques with our modeling approach, applied to high-quality digitalized images (Cerutti et al, 2017) would be a way to challenge some of the results exposed here, such as, the dependency of microtubule anisotropy α_ϕ on the mean stress f_0. It could also help estimate the transduction coefficient γ which plays a central role in the sensitivity of the feedback mechanism. This could constitute a fruitful line of future work.

Finally, our model raises further questions about the dynamics of microfibrils. The latter is described by Eq. (7) that contains a degradation term. This term is required mathematically for the existence of a steady regime. Without it, the cell wall would undergo ceaseless accumulation of cellulose. Whether such a limiting term has an enzymatic origin or could be explained by a growth-related dilution/advection process remains to be established. It is in fact not self-evident that growth-induced advection/diffusion could suffice for rapid changes in growth direction (as observed during organ initiation). Indeed, in principle, newly deposited microfibrils would be in mechanical competition with older layers with different orientation. This competition would further slow the mechanical responsiveness of the tissue down. In depth theoretical modeling should provide further insights into this problem.

A The tensor ramp function

Here the tensor function $(\,\cdot\,)_+$ is defined on the set of the symmetric second order tensors. For such tensor $\boldsymbol{T}$ (of dimension d), the tensor rank decomposition of $\boldsymbol{T}$ reads:

$$\boldsymbol{T} = \sum_{n=1}^{d} \lambda_n \boldsymbol{t}_n \otimes \boldsymbol{t}_n$$

where λ_n are the eigenvalues of $\boldsymbol{T}$, and $\boldsymbol{t}_n$ are corresponding normalized eigenvectors. We define:

$$(\boldsymbol{T})_+ = \sum_{n=1}^{d} \max\left(\lambda_n, 0\right) \boldsymbol{t}_n \otimes \boldsymbol{t}_n,$$

which assures that $(\boldsymbol{T})_+$ is a positive symmetric tensor.

B The stiffness tensor as a function of the microfibril distribution

This appendix details Eq. (6), that establishes a relation between the fiber organization and the associated stiffness, as described in Cox (1952) .

We consider that microfibrils behave like linear springs (of rest length l_0 and stiffness k). Moreover, by assuming affine deformation, their deformation reads:

$$\frac{\Delta l\left(\theta\right)}{l_0} \simeq \boldsymbol{e}_\theta \cdot \left(\boldsymbol{E} \cdot \boldsymbol{e}_\theta\right) = \boldsymbol{E} : \boldsymbol{e}_\theta \otimes \boldsymbol{e}_\theta = \boldsymbol{E} : \boldsymbol{\Theta}.$$

where $\Theta = e_\theta \otimes e_\theta$ is the projector on direction θ ('$\otimes$' depicts the tensor outer product). The previous expression yields the total stretching energy density per unit volume of fibers (summed over all directions):

$$u = \frac{1}{2} Y_f \int_\pi \mathrm{d}\theta \rho(\theta) (E : \Theta)^2 = \frac{1}{2} E : Y_f \int_\pi \mathrm{d}\theta \rho(\theta) \Theta \otimes \Theta : E \qquad (17)$$

with:

$$Y_f = \frac{k l_0^2}{h}$$

(where h is the wall's thickness). Deriving twice the energy yields the stiffness tensor:

$$\mathbb{C}_f = \frac{\partial^2 u}{\partial^2 E} = Y_f \int_\pi \mathrm{d}\theta \rho(\theta) \Theta \otimes \Theta$$

or in the basis (e_x, e_y):

$$(\mathbb{C}_f)_{ijkl} = Y_f \int_\pi \mathrm{d}\theta \rho(\theta) \cos(\theta)^{\Delta_{ijkl}} \sin(\theta)^{4 - \Delta_{ijkl}}$$

with $\Delta_{ijkl} = \delta_{i,1} + \delta_{j,1} + \delta_{k,1} + \delta_{l,1}$, where '$\delta$' stands for the Kronecker delta function. Linearizing the cosine-sine products yields an expression of $\mathbb{C}_f$ involving the 0th, 1st and 2nd order Fourier coefficients:

$$[\mathbb{C}_f] = \frac{\pi Y_f \rho_0}{16} \begin{bmatrix} 3 + \frac{\rho_2 + 4\rho_1}{\rho_0} & 1 - \frac{\rho_2}{\rho_0} & \frac{2\tilde{\rho}_1 + \tilde{\rho}_2}{\rho_0} \\ 1 - \frac{\rho_2}{\rho_0} & 3 + \frac{\rho_2 - 4\rho_1}{\rho_0} & \frac{2\tilde{\rho}_1 - \tilde{\rho}_2}{\rho_0} \\ \frac{2\tilde{\rho}_1 + \tilde{\rho}_2}{\rho_0} & \frac{2\tilde{\rho}_1 - \tilde{\rho}_2}{\rho_0} & 1 - \frac{\rho_2}{\rho_0} \end{bmatrix}$$

where, for any natural number n:

$$\hat{\rho}_n = \int_\pi \frac{\mathrm{d}\theta}{\pi} \rho(\theta) e^{-2in\theta} \quad \text{and} \quad (\rho_n, \tilde{\rho}_n) = 2 (\Re(\hat{\rho}_n), -\Im(\hat{\rho}_n)).$$

C Modeling cellulose deposition *via* CSC trajectories

We here develop a kinetic model for CSC-microtubule binding, providing a chemical background to the cellulose deposition model. Here, cellulose deposition is controlled through the orientation of the CSC trajectories depicted by an *a priori* non-uniform π-periodic distribution $\mu(\theta)$ that depicts the trajectories of proteins (regardless of their sense).

$$\mathrm{d}_t \rho(\theta) = k_\rho^0 \mu(\theta) - k_\rho' \rho(\theta), \qquad (18)$$

We assume that a constant pool of CSCs is available, characterized by a constant concentration μ_{tot}. Proteins can be either free or bound to a microtubule. The free proteins are assumed to follow individual Brownian trajectories within the membrane bi-layer; for that the related cellulose deposition is isotropic, characterized by a concentration μ_{free}. The contribution of the bound proteins is characterized by the distribution $\mu_{\text{bound}}(\theta)$ that depicts the trajectories of proteins on microtubules. We assume that CSCs are active regardless of their binding state, implying that cellulose deposition occurs even in the absence of microtubules (Emons et al, 2007). Microtubules solely introduce a bias in the distribution of trajectories μ. The total concentration of CSCs reads:

$$\int_\pi \mu = \mu_{\text{free}} + \int_\pi \mu_{\text{bound}} = \mu_{\text{tot}}. \qquad (19)$$

The kinetics of CSC-microtubule binding is modeled by a multiplicative coupling between the concentration of microtubules in a given direction θ and the concentration of available free proteins, along with an isotropic liberation rate:

$$\mathrm{d}_t \mu_{\text{bound}}(\theta) = k_\mu \mu_{\text{free}} \phi^\infty (S, \theta) - k_\mu' \mu_{\text{bound}}(\theta) \qquad (20)$$

where k_μ and k'_μ are kinetic constants. Eqs. (19) and (20) lead to the steady-state expression:

$$\mu_{\text{bound}}^\infty(\theta) = \mu_{\text{tot}} \cdot \frac{K_\mu \phi^\infty(\boldsymbol{S}, \theta)}{1 + K_\mu \int_\pi \phi^\infty} \tag{21}$$

where $K_\mu = k_\mu / k'_\mu$ depicts the affinity of CSCs for microtubules. By combining the previous steady-state distribution of CSCs with the expression of cellulose deposition (Eq. (18)), we obtain:

$$\mathrm{d}_t \rho(\theta) = k_\rho^0 \mu_{\text{tot}} \cdot \frac{1 + K_\mu \phi^\infty(\boldsymbol{S}, \theta)}{1 + K_\mu \int_\pi \phi^\infty} - k'_\rho \rho(\theta) \tag{22}$$

that can be roughly simplified to obtain Eq. (7) by assuming that for all θ, $K_\mu \phi^\infty(\boldsymbol{S}, \theta) \gg 1$ (strong affinity):

$$\mathrm{d}_t \rho(\theta) = k_\rho^0 \mu_{\text{tot}} \cdot \frac{\phi^\infty(\boldsymbol{S}, \theta)}{\int_\pi \phi^\infty} - k'_\rho \rho(\theta). \tag{23}$$

The product $k_\rho^0 \mu_{\text{tot}}$ defines the kinetic constant k_ρ used in the main text.

D Details about the specific expression of the microtubule depolymerization probability

Eq. (10) derives from Arrhenius law: a chemical reaction rate (k_A hereafter) is a direct function of its activation energy, *i.e.* the energetic barrier (E_A) the system has to overcome to go from one chemical state to another:

$$k_A = k_0 e^{-\frac{E_A}{RT}}.$$

The product RT corresponds to the thermal energy of the considered molecules are embedded in (R and T respectively stand for the Arrhenius constant and the absolute temperature).

This general experimental law has been amended latter on in the context of biochemistry and cell adhesion in the following way (Bell, 1978). The energy barrier molecules have to overcome can be lowered or raised when mechanical forces are applied to them. The resulting expression reads:

$$k_B = k_0 e^{-\frac{E_A \pm \alpha f}{RT}}$$

where f depicts the force applied to the considered molecules and $\pm \alpha$ stands as a coupling parameter. Clearly, the sign of this coupling parameter depends on the action of the force: if the latter eases the reaction, then the coupling parameter must be negative, so the activation barrier is lowered and the transition rate is increased.

Our working hypothesis is that mechanical forces applied to microtubules reduce their depolymerization rate; we therefore postulated a positive coupling parameters. Simplifying the notation as follows:

$$\begin{cases} k'_\phi{}^0 := k_0 e^{-\frac{E_A}{RT}} \\ \gamma := \frac{\alpha}{RT} \end{cases}$$

and considering that E_A is proportional to force, leads to Eq. (10).

E Microtubule principal axis and anisotropy at steady regime

Generally, the microtubule distribution ϕ is summarized through the angle of its mean orientation (θ_ϕ) and through its anisotropy (α_ϕ), respectively given by:

$$\theta_\phi = -\frac{\arg \hat{\phi}_1}{2} \quad \text{and} \quad \alpha_\phi = \frac{|\hat{\phi}_1|}{\hat{\phi}_0} \tag{24}$$

where 'arg' is the complex argument, and $\{\hat{\phi}_n\}_{n \in \mathbb{N}}$ depict the Fourier coefficients of ϕ. We define θ_ρ and α_ρ in the same way, using the microfibril distribution ρ.

The steady-state Fourier sequence of microtubules is derived from Eq. (11) and read:

$$\forall n \in \mathbb{N}: \quad \hat{\phi}_n^\infty = \frac{c_0}{\pi} \frac{I_n\left(2\gamma|\hat{f}_1|\right)}{\frac{e^{-\gamma f_0}}{\pi K_\phi} + I_0\left(2\gamma|\hat{f}_1|\right)} e^{-2in\theta_S} \tag{25}$$

where θ_S depicts the angle of main stress, and where functions $\{I_n\}_{n\in\mathbb{N}}$ depict the modified Bessel functions of the first kind (Abramowitz and Stegun, 1972):

$$\forall n \in \mathbb{N}, \forall x \in \mathbb{R}: I_n\left(x\right) = \int_\pi \frac{\mathrm{d}\theta}{\pi} e^{x\cos\theta} \cos n\theta.$$

By expressing the complex argument of $\hat{\phi}_1$ from the previous expression, one sees that $\theta_\phi^\infty = \theta_S$. This means that microtubules align with the main direction of stress. This alignment is moreover symmetric, according to this direction (with the parametrization $\theta \leftarrow \theta - \theta_S$, the imaginary part of the Fourier coefficients vanishes).

The anisotropy ratio α_ϕ^∞ (Fig. 3(b)) reads:

$$\alpha_\phi^\infty = \frac{I_1\left(2\gamma|\hat{f}_1|\right)}{I_0\left(2\gamma|\hat{f}_1|\right)}. \tag{26}$$

which is a growing function of $|\hat{f}_1|$ (if $\gamma > 0$). According to the previous expression, the steady-state anisotropy of microtubules depends on stress only, and not on the chemical kinetics.

F Details on the simulation pipeline

We detail the numerical procedure employed in Section 3.3. All simulations have been performed in the framework presented in (Boudon et al, 2015), based on the open-source softwares *Sofa* (Faure et al, 2012) and *OpenAlea* (Pradal et al, 2008). The numerical procedure employed in this paper is adapted from Boudon et al (2015).

F.1 Mechanical equilibrium

F.1.1 Space discretization

Finite element procedure We discretize the continuous model through triangular finite elements. Current material positions x are expressed according to the mesh nodes x_i based on a Lagrange $\mathbb{P}_1$ barycentric interpolation:

$$x = \sum_i \xi^i\left(X\right) x_i$$

where $\xi^i\left(X\right)$ depicts the barycentric shape function associated with node i and evaluated at X, the 2D barycentric coordinates of the material point in the reference configuration. Spatial differentiation yields one 3×2 barycentric deformation gradient tensors per triangle e:

$$F_e = \sum_i x_i \otimes \nabla_X \xi^i\left(X\right) \tag{27}$$

(operator $'\otimes'$ depicts the vector outer product, $a \otimes b = a \cdot b^T$). The 2D Green-Lagrangian strain tensor and the second Piola-Kirchhoff stress are derived from F according to:

$$E_e = \frac{1}{2}\left(F_e^T \cdot F_e - I\right) \quad \text{and} \quad S_e = \mathbb{C}_{w,e} : E_e,$$

yielding the internal energy of the system (that is only due to deformation):

$$U = \frac{h}{2} \sum_e \mathcal{A}_e E_e : S_e = \frac{h}{2} \sum_e \mathcal{A}_e E_e : \mathbb{C}_{w,e} : E_e,$$

where h and $\mathcal{A}_e$ respectively stand for the wall thickness (that is uniform) and the surface of triangle e. Nodal inner forces are obtained by considering the infinitesimal work due to an infinitesimal displacement of the node, which, by virtue of the first law of thermodynamics (in adiabatic conditions), leads to:

$$f_i^{\text{int}} = -\frac{\partial U}{\partial x_i}. \tag{28}$$

The inner forces are derived from pressure and expressed at each node v according to its adjacent triangles $\mathcal{T}(v)$:

$$f_v^P = \frac{P}{3} \sum_{e \in \mathcal{T}(v)} \mathcal{A}_e n_e,$$

where n_e stands for the outer normal of triangle e.

Meshes All meshes have been generated through the open source software *Blender* www.blender.org. At the exception of the cylindrical stem (for which the original mesh was satisfactory), they have been enhanced *via* a surface smoothing procedure implemented in the non-commercial meshing tool *Graphite* (alice.loria.fr/software/graphite).

F.1.2 Time discretization

Computing the equilibrium (Eq. (3)) consists in minimizing the total energy U (see Boudon et al, 2015, for further details). This is performed dynamically by writing the quasi-static law of motion for each node i:

$$f_i^P + f_i^{\text{int}} \simeq \mu \frac{\mathrm{d}x_i}{\mathrm{d}t}$$

(where μ is a damping coefficient that can be integrated into the time step). The previous equation is solved implicitly with the conjugate gradient algorithm.

To improve stability and to avoid excessive stiffness inhomogeneity, the tensor S employed in Eq. 11 is modified on each element and integrates a weighted average of the neighboring stress tensors.

F.2 Dynamical resolution of Eq. 7

The dynamics of the microfibril distribution is computed by an iterative update of the first three Fourier coefficients of ρ through the following forward Euler time scheme with constant time step Δt (Eq. 7 and Fig. 8):

$$\forall n: \quad \hat{\rho}_n^{t+\Delta t} = \left(1 - k_\rho' \Delta t\right) \hat{\rho}_n^t + \frac{2 k_\rho \Delta t}{\pi} \frac{\hat{\phi}_n^\infty\left(S^t\right)}{\phi_0^\infty\left(S^t\right)}. \tag{29}$$

The stiffness tensor $\mathbb{C}_w$ is subsequently updated according to Eqs. 4 to 6 and 25.

At $t = t_0$, the system is set to its null-stress equilibrium, derived from Eqs. 11 and 14:

$$\phi(\theta, t_0) = \frac{c_0 K_\phi}{1 + K_\phi \pi} \quad \text{and} \quad \rho(\theta, t_0) = \frac{K_\rho}{\pi}. \tag{30}$$
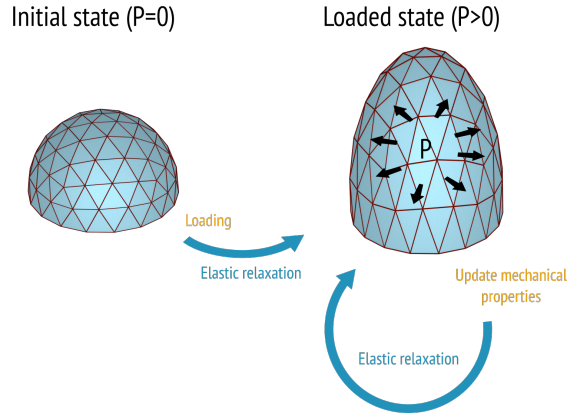
Fig. 8 Simulation pipeline. The initial state corresponds to the null stress state (no residual stress and no loading). The elastic equlibrium is computed after loading the structure with pressure $P > 0$. At each elastic equilibrium, the mechanical properties are updated, which brings the systems out of equilibrium.

F.3 Visualization of the microfibril distributions in Figs. 5 to 7

We adapted the concept of nematic tensor from the physics of liquid crystals (De Gennes and Prost, 1995) by defining:

$$Q_\phi = 4 \int_\pi \frac{\mathrm{d}\theta}{\pi} \phi(\theta) \, \Theta = \phi_0 \begin{bmatrix} 1 + \frac{\phi_1}{\phi_0} & \frac{\tilde{\phi}_1}{\phi_0} \\ \frac{\tilde{\phi}_1}{\phi_0} & 1 - \frac{\phi_1}{\phi_0} \end{bmatrix}. \tag{31}$$

Notice that, as stated in 3.1, the previous definition builds a formal equivalence between the definition of anisotropy based on Fourier coefficients (Eqs. (13) and (24)) and the nematic-based ratio employed in Boudaoud et al (2014) (Eq. (12)). In fact, the matrix expression of Q_ϕ becomes diagonal in the basis associated with the rotation that zeroes the odd Fourier coefficient $\tilde{\phi}_1$ (in this basis $|\hat{\phi}_1| = \hat{\phi}_1 = \phi_1/2 \in \mathbb{R}^+$). Since $|\hat{\phi}_1|$ and ϕ_0 are base-invariant, the two eigenvalues of Q_ϕ are equal to $\phi_0 \pm 2|\hat{\phi}_1|$, which gives:

$$\frac{Q_{\phi,1} - Q_{\phi,2}}{Q_{\phi,1} + Q_{\phi,2}} = \frac{2|\hat{\phi}_1|}{\phi_0} = \frac{|\hat{\phi}_1|}{\hat{\phi}_0} \tag{32}$$

Q_ϕ is equivalent to an ellipse with main axis oriented by $\theta_\phi = -1/2 \arg \hat{\phi}_1$ (Eq. 24), and with aspect ratio and semi-major axis respectively given by $(1 - \alpha_\phi) / (1 + \alpha_\phi)$ (with $\alpha_\phi = |\hat{\phi}_1|/\hat{\phi}_0$) and $\phi_0 (1 + \alpha_\phi)$ (see Fig. 9).

References

Abramowitz M, Stegun I (1972) Handbook of mathematical functions. NY: Dover Publications

Ali O, Mirabet V, Godin C, Traas J (2014) Physical Models of Plant Development. Annual Review of Cell and Developmental Biology 30(1):59–78, DOI 10.1146/annurev-cellbio-101512-122410, URL http://dx.doi.org/10.1146/annurev-cellbio-101512-122410

Allard JF, Wasteneys GO, Cytrynbaum EN (2010) Mechanisms of Self-Organization of Cortical Microtubules in Plants Revealed by Computational Simulations. Molecular Biology of the Cell 21(2):278–286, DOI 10.1091/mbc.E09-07-0579, URL http://www.molbiolcell.org/content/21/2/278

Baskin TI (2005) Anisotropic expansion of the plant cell wall. Annual Review of Cell and Developmental Biology 21(1):203–222, DOI 10.1146/annurev.cellbio.20.082503.103053, URL http://dx.doi.org/10.1146/annurev.cellbio.20.082503.103053
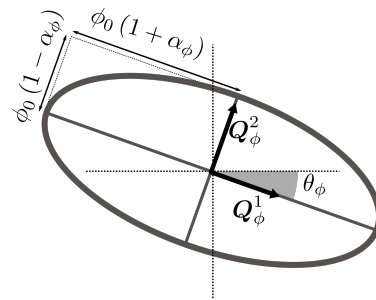
Fig. 9 Ellipse-based visualization of the nematic tensor associated with the distribution ϕ.

Beauzamy L, Louveaux M, Hamant O, Boudaoud A (2015) Mechanically, the Shoot Apical Meristem of Arabidopsis Behaves like a Shell Inflated by a Pressure of About 1 MPa. Frontiers in plant science, Frontiers in Plant Science 6, 6:1038–1038, DOI 10.3389/fpls.2015.01038,10.3389/fpls.2015.01038, URL http://europepmc.org/abstract/MED/26635855,http://europepmc.org/articles/PMC4659900/?report=abstract, 00008

Bell GI (1978) Models for the Specific Adhesion of Cells to Cells. Science 200(4342):618–627, URL http://www.jstor.org/stable/1746930, 03531

Boudaoud A, Burian A, Borowska-Wykret D, Uyttewaal M, Wrzalik R, Kwiatkowska D, Hamant O (2014) FibrilTool, an ImageJ plug-in to quantify fibrillar structures in raw microscopy images. Nature Protocols 9(2):457–463, DOI 10.1038/nprot.2014.024, URL http://www.nature.com/nprot/journal/v9/n2/full/nprot.2014.024.html

Boudon F, Chopard J, Ali O, Gilles B, Hamant O, Boudaoud A, Traas J, Godin C (2015) A Computational Framework for 3d Mechanical Modeling of Plant Morphogenesis with Cellular Resolution. PLOS Comput Biol 11(1):e1003,950, DOI 10.1371/journal.pcbi.1003950, URL http://journals.plos.org/ploscompbiol/article?id=10.1371/journal.pcbi.1003950

Bozorg B, Krupinski P, Jönsson H (2014) Stress and Strain Provide Positional and Directional Cues in Development. PLOS Comput Biol 10(1):e1003,410, DOI 10.1371/journal.pcbi.1003410, URL http://journals.plos.org/ploscompbiol/article?id=10.1371/journal.pcbi.1003410

Bozorg B, Krupinski P, Jönsson H (2016) A continuous growth model for plant tissue. Physical Biology 13(6):065,002, DOI 10.1088/1478-3975/13/6/065002, URL http://stacks.iop.org/1478-3975/13/i=6/a=065002, 00000

Braybrook SA, Peaucelle A (2013) Mechano-Chemical Aspects of Organ Formation in Arabidopsis thaliana : The Relationship between Auxin and Pectin. PLOS ONE 8(3):e57,813, DOI 10.1371/journal.pone.0057813, URL http://journals.plos.org/plosone/article?id=10.1371/journal.pone.0057813

Burian A, Ludynia M, Uyttewaal M, Traas J, Boudaoud A, Hamant O, Kwiatkowska D (2013) A correlative microscopy approach relates microtubule behaviour, local organ geometry, and cell growth at the Arabidopsis shoot apical meristem. Journal of Experimental Botany p ert352, DOI 10.1093/jxb/ert352, URL http://jxb.oxfordjournals.org/content/early/2013/10/22/jxb.ert352

Burk DH, Ye ZH (2002) Alteration of Oriented Deposition of Cellulose Microfibrils by Mutation of a Katanin-Like Microtubule-Severing Protein. The Plant Cell 14(9):2145–2160, DOI 10.1105/tpc.003947, URL http://www.plantcell.org/content/14/9/2145

Cerutti G, Ali O, Godin C (2017) DRACO-STEM: An Automatic Tool to Generate High-Quality 3d Meshes of Shoot Apical Meristem Tissue at Cell Resolution. Frontiers in Plant Science 8:353, DOI 10.3389/fpls.2017.00353

Changeux JP (2012) Allostery and the Monod-Wyman-Changeux Model After 50 Years. Annual Review of Biophysics 41(1):103–133

Coen E, Rolland-Lagan AG, Matthews M, Bangham JA, Prusinkiewicz P (2004) The genetics of geometry. Proceedings of the National Academy of Sciences of the United States of America 101(14):4728–4735, DOI 10.1073/pnas.0306308101, URL http://www.pnas.org/content/101/14/4728

Corson F, Hamant O, Bohn S, Traas J, Boudaoud A, Couder Y (2009) Turning a plant tissue into a living cell froth through isotropic growth. Proceedings of the National Academy of Sciences 106(21):8453–8458, DOI 10.1073/pnas.0812493106, URL http://www.pnas.org/content/106/

21/8453

Cosgrove DJ (2001) Wall Structure and Wall Loosening. A Look Backwards and Forwards. Plant Physiology 125(1):131–134, DOI 10.1104/pp.125.1.131, URL http://www.plantphysiol.org/content/125/1/131

Cosgrove DJ (2005) Growth of the plant cell wall. Nature Reviews Molecular Cell Biology 6(11):850–861, DOI 10.1038/nrm1746, URL http://www.nature.com/nrm/journal/v6/n11/abs/nrm1746.html

Cox HL (1952) The elasticity and strength of paper and other fibrous materials. British Journal of Applied Physics 3(3):72, DOI 10.1088/0508-3443/3/3/302, URL http://stacks.iop.org/0508-3443/3/i=3/a=302

De Gennes PG, Prost J (1995) The physics of liquid crystals. Oxford university press

Delingette H (2008) Triangular springs for modeling nonlinear membranes. IEEE transactions on visualization and computer graphics 14(2):329–341, DOI 10.1109/TVCG.2007.70431

Dixit R, Cyr R (2004) Encounters between Dynamic Cortical Microtubules Promote Ordering of the Cortical Array through Angle-Dependent Modifications of Microtubule Behavior. The Plant Cell 16(12):3274–3284, DOI 10.1105/tpc.104.026930, URL http://www.plantcell.org/content/16/12/3274

Dumais J, Shaw SL, Steele CR, Long SR, Ray PM (2006) An anisotropic-viscoplastic model of plant cell morphogenesis by tip growth. The International journal of developmental biology 50(2-3):209–222, URL http://cat.inist.fr/?aModele=afficheN&cpsidt=17584781

Dupuy L, Mackenzie JP, Haseloff JP (2006) A biomechanical model for the study of plant morphogenesis: Coleocheate orbicularis, a 2d study species. In: Proceedings of the 5th Plant Biomechanics Conference, Stockholm, Sweden

Dyson RJ, Jensen OE (2010) A fibre-reinforced fluid model of anisotropic plant cell growth. Journal of Fluid Mechanics 655:472–503, DOI 10.1017/S002211201000100X, URL http://www.journals.cambridge.org/abstract_S002211201000100X

Dyson RJ, Band LR, Jensen OE (2012) A model of crosslink kinetics in the expanding plant cell wall: Yield stress and enzyme action. Journal of Theoretical Biology 307:125–136, DOI 10.1016/j.jtbi.2012.04.035, URL http://www.sciencedirect.com/science/article/pii/S0022519312002251

Emons AMC, Höfte H, Mulder BM (2007) Microtubules and cellulose microfibrils: how intimate is their relationship? Trends in Plant Science 12(7):279–281, DOI 10.1016/j.tplants.2007.06.002, URL http://www.sciencedirect.com/science/article/pii/S1360138507001331

Erickson RO (1976) Modeling of plant growth. Annual Review of Plant Physiology 27(1):407–434

Faure F, Duriez C, Delingette H, Allard J, Gilles B, Marchesseau S, Talbot H, Courtecuisse H, Bousquet G, Peterlik I, et al (2012) Sofa: A multi-model framework for interactive physical simulation. In: Soft Tissue Biomechanical Modeling for Computer Assisted Surgery, Springer, pp 283–321

Fozard JA, Lucas M, King JR, Jensen OE (2013) Vertex-element models for anisotropic growth of elongated plant organs. Front Plant Sci 4, DOI 10.3389/fpls.2013.00233, URL http://www.ncbi.nlm.nih.gov/pmc/articles/PMC3706750/

Gelder AV (1998) Approximate Simulation of Elastic Membranes by Triangulated Spring Meshes. Journal of Graphics Tools 3(2):21–41, DOI 10.1080/10867651.1998.10487490, URL http://dx.doi.org/10.1080/10867651.1998.10487490

Ghanti D, Patra S, Chowdhury D (2016) Theory of strength and stability of kinetochore-microtubule attachments: collective effects of dynamic load-sharing. arXiv preprint arXiv:160508944

Goriely A, Amar MB (2007) On the definition and modeling of incremental, cumulative, and continuous growth laws in morphoelasticity. Biomechanics and Modeling in Mechanobiology 6(5):289–296, DOI 10.1007/s10237-006-0065-7, URL https://link.springer.com/article/10.1007/s10237-006-0065-7

Hamant O, Traas J (2010) The mechanics behind plant development. New Phytologist 185(2):369–385, DOI 10.1111/j.1469-8137.2009.03100.x, URL http://onlinelibrary.wiley.com/doi/10.1111/j.1469-8137.2009.03100.x/abstract

Hamant O, Heisler MG, Jönsson H, Krupinski P, Uyttewaal M, Bokov P, Corson F, Sahlin P, Boudaoud A, Meyerowitz EM, Couder Y, Traas J (2008) Developmental Patterning by Mechanical Signals in Arabidopsis. Science 322(5908):1650–1655, DOI 10.1126/science.1165594, URL http://www.sciencemag.org/content/322/5908/1650

Hervieux N, Dumond M, Sapala A, Routier-Kierzkowska AL, Kierzkowski D, Roeder AHK, Smith RS, Boudaoud A, Hamant O (2016) A mechanical feedback restricts sepal growth and shape in arabidopsis. Current Biology 26(8):1019–1028, DOI 10.1016/j.cub.2016.03.004, URL http://www.sciencedirect.com/science/article/pii/S0960982216301804

Kennaway R, Coen E, Green A, Bangham A (2011) Generation of Diverse Biological Forms through Combinatorial Interactions between Tissue Polarity and Growth. PLOS Comput Biol 7(6):e1002,071, DOI 10.1371/journal.pcbi.1002071, URL http://journals.plos.org/ploscompbiol/article?id=10.1371/journal.pcbi.1002071

Kutschera U (1991) Regulation of cell expansion. The cytoskeletal basis of plant growth and form Academic Press, London pp 149–158

Landau LD, Lifshitz E (1986) Theory of Elasticity, vol 7. Elsevier, New York

Landrein B, Hamant O (2013) How mechanical stress controls microtubule behavior and morphogenesis in plants: history, experiments and revisited theories. The Plant Journal 75(2):324–338, DOI 10.1111/tpj.12188, URL http://onlinelibrary.wiley.com/doi/10.1111/tpj.12188/abstract

Lockhart JA (1965) An analysis of irreversible plant cell elongation. Journal of Theoretical Biology 8(2):264–275, DOI 10.1016/0022-5193(65)90077-9, URL http://www.sciencedirect.com/science/article/pii/0022519365900779

Nicolas A, Geiger B, Safran SA (2004) Cell mechanosensitivity controls the anisotropy of focal adhesions. Proceedings of the National Academy of Sciences of the United States of America 101(34):12,520–12,525

Ortega JKE (1985) Augmented Growth Equation for Cell Wall Expansion. Plant Physiology 79(1):318–320, DOI 10.1104/pp.79.1.318, URL http://www.plantphysiol.org/content/79/1/318

Paredez AR, Somerville CR, Ehrhardt DW (2006) Visualization of Cellulose Synthase Demonstrates Functional Association with Microtubules. Science 312(5779):1491–1495, DOI 10.1126/science.1126551, URL http://science.sciencemag.org/content/312/5779/1491

Peaucelle A, Braybrook SA, Le Guillou L, Bron E, Kuhlemeier C, Höfte H (2011) Pectin-induced changes in cell wall mechanics underlie organ initiation in arabidopsis. Current Biology 21(20):1720–1726, DOI 10.1016/j.cub.2011.08.057, URL http://www.sciencedirect.com/science/article/pii/S0960982211009638

Pradal C, Dufour-Kowalski S, Boudon F, Fournier C, Godin C (2008) OpenAlea: a visual programming and component-based software platform for plant modelling. Functional Plant Biology 35(10):751–760, URL http://dx.doi.org/10.1071/FP08084

Rojas ER, Hotton S, Dumais J (2011) Chemically Mediated Mechanical Expansion of the Pollen Tube Cell Wall. Biophysical Journal 101(8):1844–1853, DOI 10.1016/j.bpj.2011.08.016, URL http://www.sciencedirect.com/science/article/pii/S0006349511009623

Sampathkumar A, Krupinski P, Wightman R, Milani P, Berquand A, Boudaoud A, Hamant O, Jönsson H, Meyerowitz EM (2014a) Subcellular and supracellular mechanical stress prescribes cytoskeleton behavior in Arabidopsis cotyledon pavement cells. eLife 3:e01,967, DOI 10.7554/eLife.01967, URL http://elifesciences.org/content/3/e01967v1

Sampathkumar A, Yan A, Krupinski P, Meyerowitz EM (2014b) Physical Forces Regulate Plant Development and Morphogenesis. Current Biology 24(10):R475–R483, DOI 10.1016/j.cub.2014.03.014, URL http://www.sciencedirect.com/science/article/pii/S0960982214002735

Sassi M, Ali O, Boudon F, Cloarec G, Abad U, Cellier C, Chen X, Gilles B, Milani P, Friml J, Vernoux T, Godin C, Hamant O, Traas J (2014) An Auxin-Mediated Shift toward Growth Isotropy Promotes Organ Formation at the Shoot Meristem in Arabidopsis. Current Biology 24(19):2335–2342, DOI 10.1016/j.cub.2014.08.036, URL http://linkinghub.elsevier.com/retrieve/pii/S0960982214010495

Tindemans SH, Hawkins RJ, Mulder BM (2010) Survival of the Aligned: Ordering of the Plant Cortical Microtubule Array. Physical Review Letters 104(5):058,103, DOI 10.1103/PhysRevLett.104.058103, URL http://link.aps.org/doi/10.1103/PhysRevLett.104.058103

Tsugawa S, Hervieux N, Hamant O, Boudaoud A, Smith RS, Li CB, Komatsuzaki T (2016) Extracting Subcellular Fibrillar Alignment with Error Estimation: Application to Microtubules. Biophysical Journal 110(8):1836–1844, DOI 10.1016/j.bpj.2016.03.011, URL http://www.sciencedirect.com/science/article/pii/S0006349516300601

Uyttewaal M, Burian A, Alim K, Landrein B, Borowska-Wykret D, Dedieu A, Peaucelle A, Ludynia M, Traas J, Boudaoud A, Kwiatkowska D, Hamant O (2012) Mechanical Stress Acts via Katanin to Amplify Differences in Growth Rate between Adjacent Cells in Arabidopsis. Cell 149(2):439–451, DOI 10.1016/j.cell.2012.02.048, URL http://www.sciencedirect.com/science/article/pii/S0092867412002899

Williamson R (1990) Alignment of Cortical Microtubules by Anisotropic Wall Stresses. Functional Plant Biology 17(6):601–613, URL http://www.publish.csiro.au/paper/PP9900601

Wolf S, Hmaty K, Höfte H (2012) Growth Control and Cell Wall Signaling in Plants. Annual Review of Plant Biology 63(1):381–407, DOI 10.1146/annurev-arplant-042811-105449, URL `https://doi.org/10.1146/annurev-arplant-042811-105449`